Available online at www.sciencedirect.com

ScienceDirect

Acta Materialia 89 (2015) 364–373

Acta MATERIALIA

www.elsevier.com/locate/actamat

Solute redistribution and phase stability at FeCr/TiO_{2-x} interfaces under ion irradiation

Y. Xu,[a,b,3] J.A. Aguiar,[a,1,3] S.K. Yadav,[a,3] O. Anderoglu,[a] J.K. Baldwin,[c] Y.Q. Wang,[a] J.A. Valdez,[a] A. Misra,[c,2] H.M. Luo,[b] B.P. Uberuaga[a] and N. Li[c,*]

[a] *Materials Science and Technology Division, MST-8, Los Alamos National Laboratory, Los Alamos, NM 87545, USA*
[b] *Department of Chemical and Materials Engineering, New Mexico State University, Las Cruces, NM 88003, USA*
[c] *Materials Physics and Applications Division, MPA-CINT, Los Alamos National Laboratory, Los Alamos, NM 87545, USA*

Received 1 September 2014; revised 11 January 2015; accepted 28 January 2015

Abstract—Cr diffusion in trilayer thin films of 100 nm Fe–18Cr/125 nm TiO_{2-x}/100 nm Fe–18Cr deposited on MgO substrates at 500 °C was studied by either annealing at 500 °C or Ni^{3+} ion irradiation at 500 °C. Microchemistry and microstructure evolution at the metal/oxide interfaces were investigated using (high-resolution) transmission electron microscopy, energy-dispersive X-ray spectroscopy and electron energy loss spectroscopy. Diffusion of Cr into the O-deficient TiO_2 layer, with negligible segregation to the FeCr/TiO_{2-x} interface itself, was observed under both annealing and irradiation. Cr diffusion into TiO_{2-x} was enhanced in ion-irradiated samples as compared to annealed. Irradiation-induced voids and amorphization of TiO_{2-x} was also observed. The experimental results are rationalized using first-principles calculations that suggest an energetic preference for substituting Ti with Cr in sub-stoichiometric TiO_2. The implications of these results on the irradiation stability of oxide-dispersed ferritic alloys are discussed.
Published by Elsevier Ltd. on behalf of Acta Materialia Inc.

Keywords: Radiation-induced solute redistribution (RISR); Metal/oxide interface; Density functional theory (DFT)

1. Introduction

Radiation-induced solute redistribution (RISR) is a prevalent issue within the nuclear materials community [1–4]. It originates from a preferential association of solutes with irradiation-generated point defects [5] and how they interact with interfaces [6]. The ensuing consequence is the change in the local chemical composition of the material, with enrichment of some and depletion of other solutes near point defect sinks such as interfaces [7]. The diffusion behavior of the element Cr, one of the major components in steels, has attracted tremendous attention [7–10]. Through forming α′ or a variety of intermetallic phases [10,11], Cr aggregates at grain boundaries (GBs) in ferritic martensitic steels under irradiation, which can embrittle the alloy. On the contrary, radiation-induced Cr depletion has been revealed in fcc austenitic steels, which is the major cause of irradiation assisted stress corrosion cracking [9,12]. Although the corresponding mechanisms have been explored by both atomic-scale modeling and experiments, a complete understanding of Cr diffusion, especially in complex alloys and composites, is still lacking. The complexity of RISR is synergistic with a number of factors, including irradiation fluence and flux, temperature, alloy composition, and the binding and diffusion energetics of Cr with vacancies/interstitials [9]. This study will focus on the diffusive behavior of element Cr under irradiation.

By dispersing nanosized oxide particles in steels, the radiation-induced swelling resistance of steel can be improved greatly. The high-density of metal/oxide interfaces in such a material act as sinks for enhancing the recombination of vacancies and self-interstitials [13–15]. With the flux of point defects diffusing toward the interfaces under irradiation, redistribution of chemical composition at boundaries commences. Compared to the situation at GBs, the problem of RISR at metal/oxide interfaces is complicated by the presence of oxygen. The affinity of oxygen to different metal elements may play an important factor here [16,17], causing changes in microstructure and microchemistry at metal/oxide interfaces; the corresponding sink efficiency and irradiation tolerance will be influenced accordingly [18]. The documented morphology modification is found to be strongly temperature and size dependent. For example, the average oxide particle size is

* Corresponding author. Tel.: +1 505 665 1857.; e-mail: nanli@lanl.gov

[1] Current address: Measurements and Characterization, National Renewable Energy Laboratory, Golden, CO 80401, USA.
[2] Current address: Department of Materials Science and Engineering, University of Michigan, Ann Arbor, MI 48109, USA.
[3] These authors have contributed equally to this work.

http://dx.doi.org/10.1016/j.actamat.2015.01.071
1359-6462/Published by Elsevier Ltd. on behalf of Acta Materialia Inc.

reported to decrease under heavy ion irradiation in the range of 380–700 °C [19,20], with the decrease occurring faster at higher temperature [20,21]. Knowledge of the microstructural evolution of oxide particles and their interfaces with the matrix alloy under irradiation plays an important role in predicting the in-service behavior of the material. In spite of the urgent need to resolve the linkage of RISR with interface structure, the issue of segregation at metal/oxide interfaces in ODS steels has been studied only to a small extent [22–26]. One of the major reasons for this is the challenge in probing the chemical composition of embedded three dimensional oxide nanoparticles. Atom-probe tomography (APT) has been widely applied to obtain 3D reconstructions of elemental components [26], although the extraction of quantitative chemical profiles around interfaces from APT is not straightforward. The gap in between cannot easily be bridged. Another hurdle results from the complex chemical composition of both matrix steels and oxide particles [27]. And segregation of a specific solute to the interface is often masked by trace impurities [28] or the interaction with other solutes in the matrix. Furthermore, the wide distribution of particle size adds more complication to this issue. Here, we present an approach to simplify the situation. Our methodology involves (i) deposition of layer-structured metal/oxide thin films which are a good representation for the metal/oxide interface [14,15,29]; (ii) precise control of layer thicknesses to investigate the size effects in RISR [30]; and (iii) simplifying the chemical composition of both the metal and oxide systems. In this article, we report on solute redistribution and phase stability at FeCr/TiO_2 interface under Ni ion irradiation at 500 °C. Diffusion of Cr into the oxide layer, with negligible enhanced segregation to the interface, has been observed. Upon incorporation of Cr, the oxide layer tends to become amorphous. Additionally, first-principles calculations have been performed to explain the incorporation mechanism of Cr into titania.

2. Experimental and simulation details

2.1. Experimental details

A trilayer thin film of Fe82 at.% Cr18 at.%/TiO_2/Fe82 at.% Cr18 at.% with layer thicknesses of 100, 125, 100 nm respectively was deposited on a MgO (100) substrate at 500 °C. In order to obtain condensed TiO_2, ratio

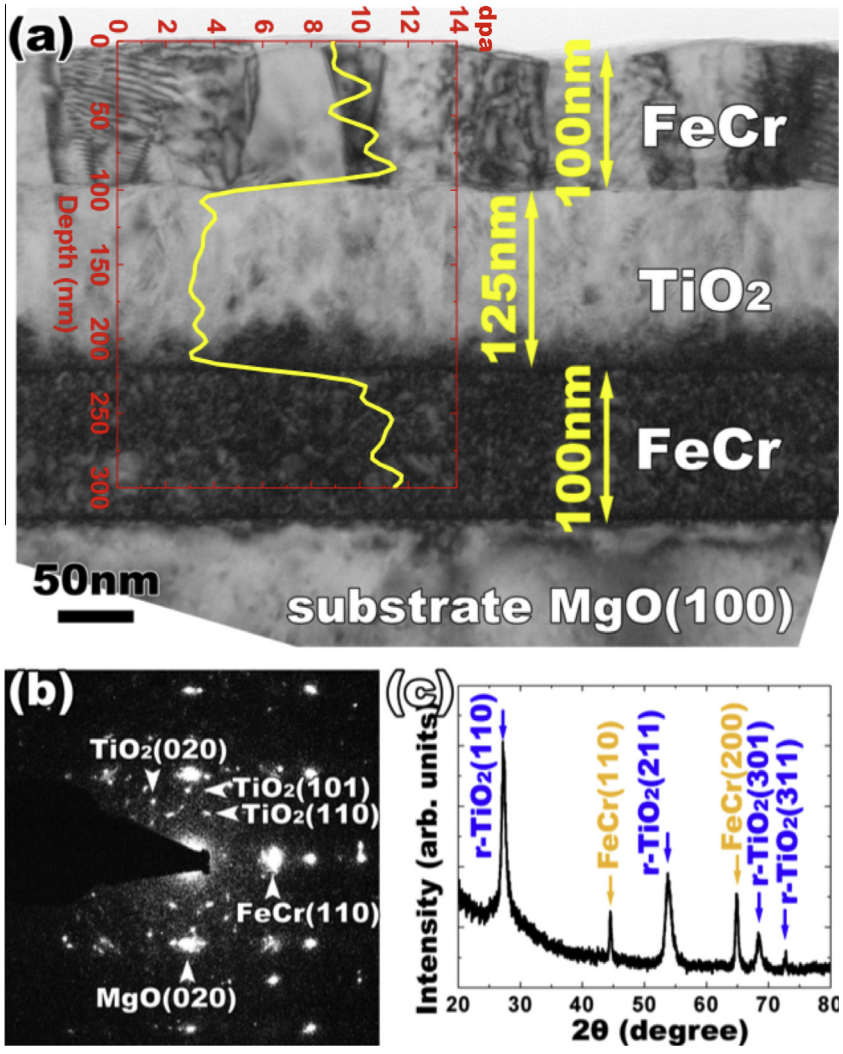

Fig. 1. (a) Bright-field XTEM image of the pristine FeCr/TiO_{2-x} trilayer thin film. Superimposed on the image is the calculated dpa profile. The average dpa is ~10 in the metal layers and ~3.5 in the oxide layer. (b) Selected area electron diffraction pattern and (c) XRD profile indicate the dominant phase in TiO_{2-x} is rutile.

frequency magnetron sputtering techniques were applied at 300 W. The deposition rate for FeCr and TiO_2 were 3 and 1 Å/s, respectively. Ion irradiation experiments were performed at the Ion Beam Materials Laboratory at the Los Alamos National Laboratory (LANL). 10 MeV Ni^{3+} ions were utilized to irradiate samples at 500 °C to a fluence of 10^{16} ions/cm^2. The elapsed time of the irradiation was ~1 h. The Monte Carlo simulation code Stopping and Range of Ions in Matter (SRIM) was used (the displacement threshold energies used for all 4 species were 25 eV while the calculations were performed in "quick" Kinchin and Pease mode) to determine the level of displacements per atom (dpa). As shown in Fig. 1a, the SRIM [31] calculated dpa profile is superimposed on the cross-sectional TEM (XTEM) micrograph: the average dpa is ~10 in the metal layers and ~3.5 in the oxide layer. For comparison, a second as-synthesized sample was annealed at 500 °C for 1 h. Analytical microscopy was performed on the image-corrected FEI Titan at LANL, operating in TEM mode at 300 keV equipped with a Gatan Tridiem electron energy loss image filter (GIF). Scanning TEM high angle annular dark field (HAADF) and electron energy loss (EEL) spectral imaging were performed using the probe-corrected FEI Titan and 100 kV Nion UltraSTEM at the Oak Ridge National Laboratory. Grazing incidence X-ray diffraction (GIXRD) measurements were performed on a Bruker AXS D8 Advance X-ray diffractometer, using Cu-Ka radiation in θ–2θ geometry, at an angle of incidence of 0.5°. The X-ray diffractometer was equipped with a Göebel mirror to achieve parallel beam diffraction optics allowing for high quality measurements on thin-films. The θ–2θ scans were performed from 10–80°, using a step size of 0.02° and a dwell time of 6 s/step.

2.2. First-principles calculation details

Substitutional defect formation energies of Cr and Fe at a Ti site in rutile TiO_2 were calculated using first-principles density functional theory (DFT). Our calculations were

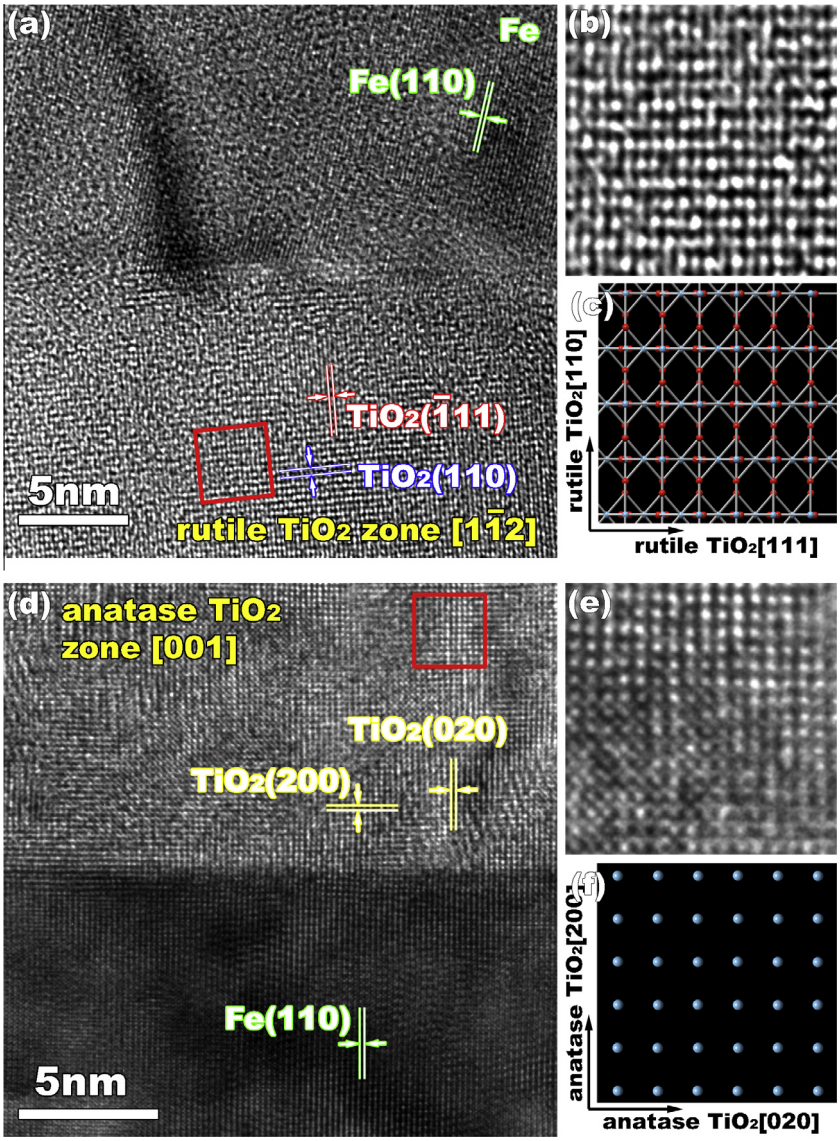

Fig. 2. (a) and (d) HRTEM images of the rutile TiO_{2-x}/FeCr heterointerface along the rutile TiO_2 [1 $\bar{1}$ 2] zone axis and the anatase TiO_{2-x}/FeCr heterointerface along the anatase TiO_2 [0 0 1] zone axis, respectively. (b) and (e) Magnified HRTEM image of rutile and anatase TiO_{2-x} indicated by the red squares in (a) and (d) respectively. (c) Ball-and-stick model of rutile TiO_2 projected along the [1 $\bar{1}$ 2] zone axes. (f) Ball model of anatase TiO_2 projected along the [0 0 1] zone axes. (For interpretation of the references to color in this figure legend, the reader is referred to the web version of this article.)

performed using the Vienna Ab initio Simulation Package (VASP) [32,33]. The DFT calculations employed the Perdew, Burke, and Ernzerhof (PBE) generalized gradient approximation (GGA) exchange–correlation functional and the projector-augmented wave (PAW) method [34]. For all calculations, a plane wave cutoff of 500 eV for the plane wave expansion of the wave functions was used to obtain highly accurate forces. The calculated crystal parameters for TiO_2 in the rutile phase were $a = b = 4.64$ Å and $c = 2.97$ Å, which are in good agreement with experimental values: $a = b = 4.59$ Å and $c = 2.95$ Å [35]. To calculate substitutional defect formation energy a $(2 \times 2 \times 3)$ supercell with 72 atoms for the rutile phase and $(2 \times 2 \times 1)$ supercell with 48 atoms for the anatase phase were used. Spin polarized calculations were considered for all cases. Force tolerance for the structural relaxation was 0.05 eV/Å.

3. Results

3.1. Microstructure and chemical analysis of pristine FeCr–TiO_{2-x} interface

The typical microstructure of the sputtered FeCr/TiO_{2-x} trilayer thin film is presented in Fig. 1a. The first FeCr layer, about 100 nm in thickness, is a single crystal with a high density of growth dislocations. The thickness of the pristine TiO_{2-x} layer is 125 nm with an average grain size of ~10 nm. Since the last FeCr layer is deposited on nanocrystalline TiO_{2-x}, the single crystalline structure cannot be maintained and the layer is polycrystalline with an average grain size of around 100 nm. Although the grain size in TiO_{2-x} is small, separated spots in the diffraction pattern (DP) in Fig. 1b indicate the preferential growth texture of the oxide. Both the DP and the XRD profile (Fig. 1c) reveal that the rutile TiO_{2-x} phase is dominant, even though the micrographs reveal a limited amount of anatase TiO_{2-x} at the interfaces (in Fig. 2). This is consistent with earlier studies that showed that low deposition pressure [36] or high temperature [37,38] favors the growth of the rutile phase. The FeCr/rutile TiO_{2-x} interfaces are characterized by multiple orientation relationships (ORs). Fig. 2a presents one typical orientation of a stepped region of the interface: along the TiO_{2-x} [1 1 2] zone axis the angle between Fe (110) and TiO_{2-x} (110) is ~70°. A magnified HRTEM image of the rutile TiO_2 (1 1 2) plane and corresponding ball-and-stick model are shown in Fig. 2b and c. For the interface between anatase TiO_{2-x} and FeCr, as shown in Fig. 2d, only one OR has been detected: TiO_{2-x} (2 0 0)||FeCr (2 0 0)||interface plane; TiO_{2-x} (0 2 0)||FeCr

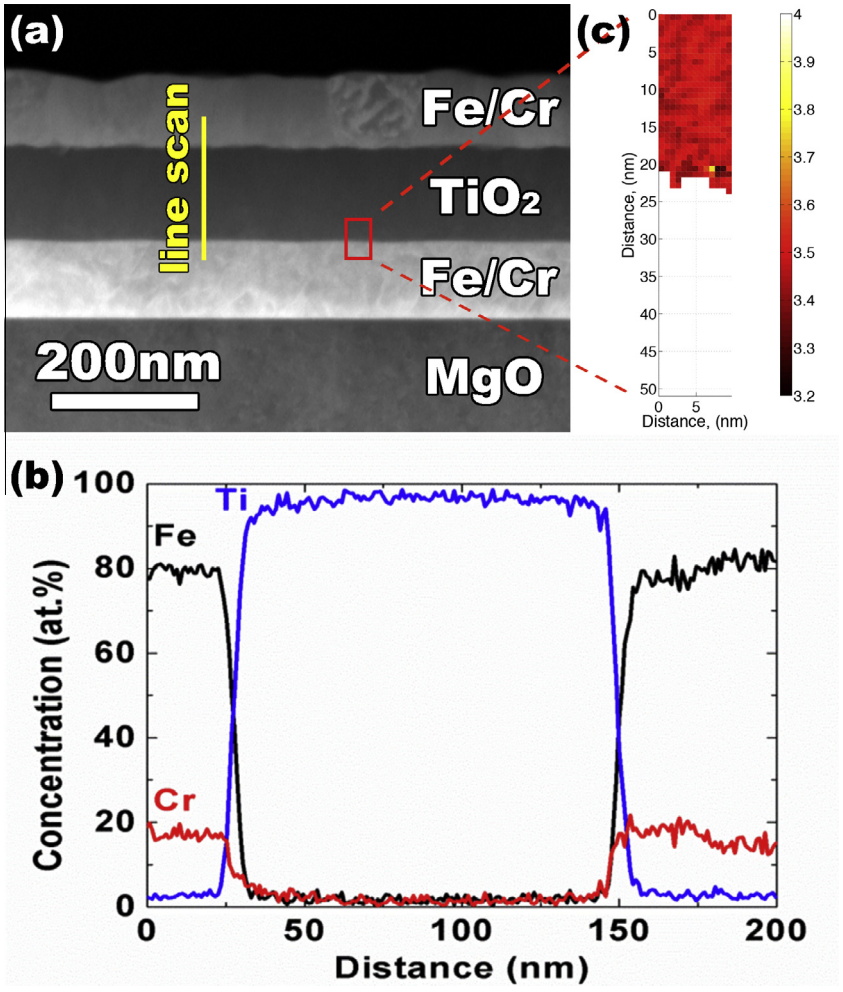

Fig. 3. Chemical analysis of the FeCr/TiO_{2-x} interface. (a) Dark field STEM image reveals a chemically abrupt interface. (b) EDS composition profiles along the line in (a) shows no intermixing of Cr, Fe or Ti across the interface. (c) Ti valence mapping, performed with EELS, also indicates a sharp interface and a slight reduced Ti valence, a sub-stoichiometric oxide. The color bar in (c) indicates the as-determined valence state of Ti.

(1 1 0). A ball model of anatase TiO_2 projected along the [0 0 1] zone axis (Fig. 2f) has been used to identify the phase structure captured by TEM (Fig. 2e).

The chemical composition of the as-grown sample was analyzed by energy dispersive X-ray spectroscopy (EDS) and electron energy loss spectroscopy (EELS), with the direction of the electron beam parallel to the interface. Fig. 3a shows a dark field STEM image of the pristine sample with TiO_{2-x} in dark contrast. Multiple line scans normal to the interface across different ORs and phases in the oxide layer were performed using EDS. A typical compositional variation along one such line scan is shown in Fig. 3b. Across the interfaces of the as-grown trilayer, there is no intermixing of Cr, Fe or Ti. This result has been verified through EELS mapping as shown in Fig. 3c. In addition, EELS analysis at both sides of the oxide layer (not shown here) revealed that the ionic valence state of Ti changes linearly from 3.5 ± 0.1 at the bottom interface plane to 3.9 ± 0.1 at the upper interface plane, indicating that the TiO_2 phase is oxygen deficient and that the degree of oxygen deficiency is greater at the lower interface than the upper interface.

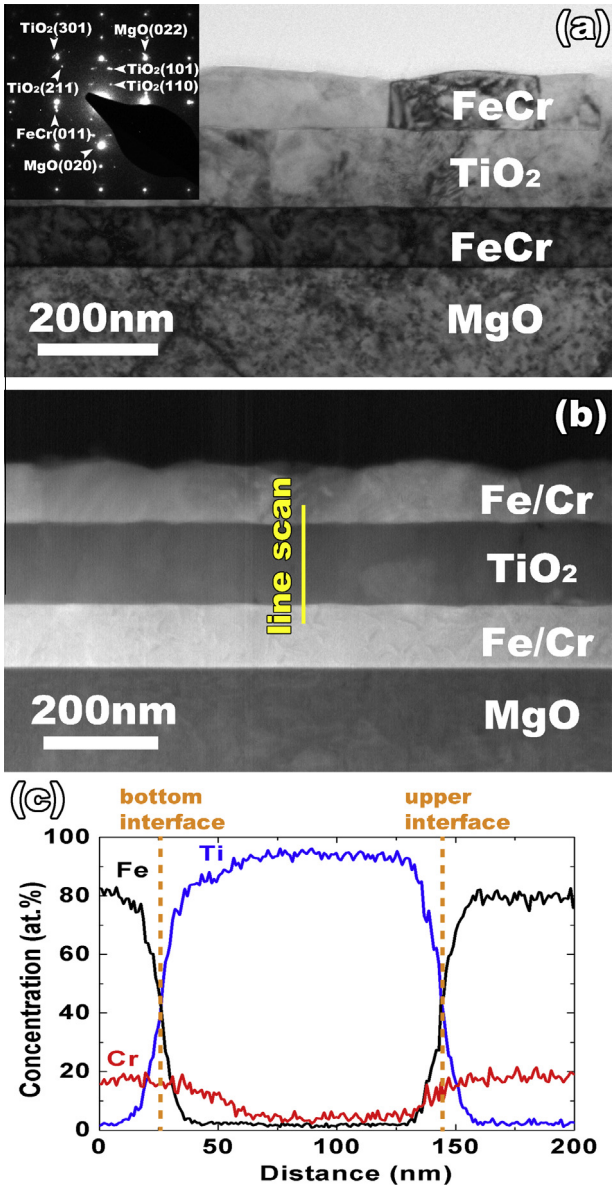

Fig. 4. (a) Cross-sectional TEM micrograph and DP show no obvious change of microstructure of the FeCr/TiO_{2-x} trilayer thin film after annealing. (b) Dark field STEM image with the position of the EDS line scan. (c) EDS composition profiles show the diffusion of Cr into the oxide layer.

3.2. Evolution of microstructure and chemical profiles across annealed FeCr/TiO_{2-x} interfaces

As a base line for comparison with the irradiated sample, one trilayer sample was annealed for one hour at 500 °C. After annealing, there is no structural change in either the FeCr or TiO_{2-x} layers. The DP in Fig. 4a reveals no formation of any new phases after annealing. However, the EDS line scan in Fig. 4c shows the diffusion of Cr into the TiO_{2-x} layer from both sides. The distance of Cr diffusing into TiO_{2-x} through the bottom interface is greater than that from the upper interface. This is correlated to the extent of substoichiometry of TiO_{2-x}, as determined by the EELS measurements mentioned above that show a greater degree of oxygen deficiency at the lower interface. As we discuss below, the ease of incorporation of Cr into the TiO_{2-x} film is directly correlated to the non-stoichiometry of TiO_{2-x}. As revealed by the shape of the Cr elemental EDS profile, there is negligible segregation at interface. That is, there is no enhancement of Cr content specifically at the interfaces.

3.3. Evolution of microstructure and chemical profiles across irradiated FeCr/TiO_{2-x} interfaces

After irradiation, both FeCr layers maintain their crystallinity. As indicated in Fig. 5, however, the TiO_{2-x} layer is comprised of both crystalline and amorphous domains, in contrast to the annealed case in which TiO_{2-x} remained crystalline. As in the annealed case, there is no clear evidence of the formation of any new chemically distinct phases (beyond the amorphous TiO_2). The structural evolution at the interface has been explored by HRTEM and, in contrast to the as-synthesized sample, no sign of anatase TiO_2 was detected. Fig. 5b and c are typical HRTEM micrographs of the structure at the interface and in the middle of the oxide layer, with the inset images of the corresponding fast Fourier transform (FFT). By comparing the corresponding diffraction halo rings, the extent of amorphization is somewhat higher at the interface region. Concurrent with the amorphization, voids are formed in the TiO_{2-x} layer with larger average sizes at the interphase boundaries than in the center of the oxide layer (as displayed in Fig. 6). Further, the thickness of oxide layer expands to 130 nm (~4% swelling) after irradiation, to accommodate the voids.

STEM studies were also carried out on the ion-irradiated multilayers. Although the interfaces between the layers are clearly distinguishable, as shown in Fig. 7a, both EELS (Fig. 7b) and EDS (Fig. 7c) chemical analyses indicate the diffusion of Cr throughout the oxide layer after irradiation. Chemical imaging of Ti, O and Fe (Fig. 7b) reveals little or no measurable intermixing across the interface. Line scans of the chemical composition have been performed at multiple regions within the sample. The shapes of the chemical profiles show negligible differences regardless of where they

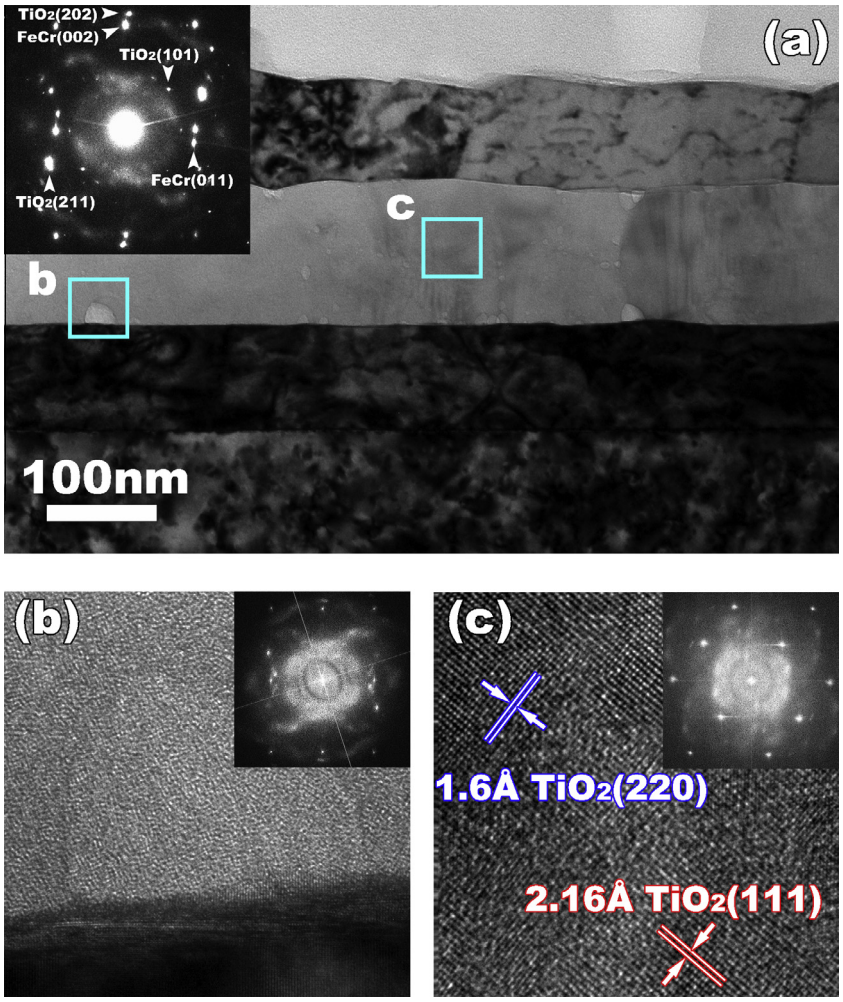

Fig. 5. (a) TEM image of the multilayer structure after irradiation with 10 MeV Ni ions. The inset shows the corresponding DP. The boxes indicate regions that are shown in higher magnification in (b) and (c). (b) Amorphous TiO_2 after irradiation; the FFT pattern (inset) indicates the amorphous nature of the material. (c) Crystalline rutile TiO_{2-x} regions (as indicated by the FFT pattern in the inset) remain after irradiation.

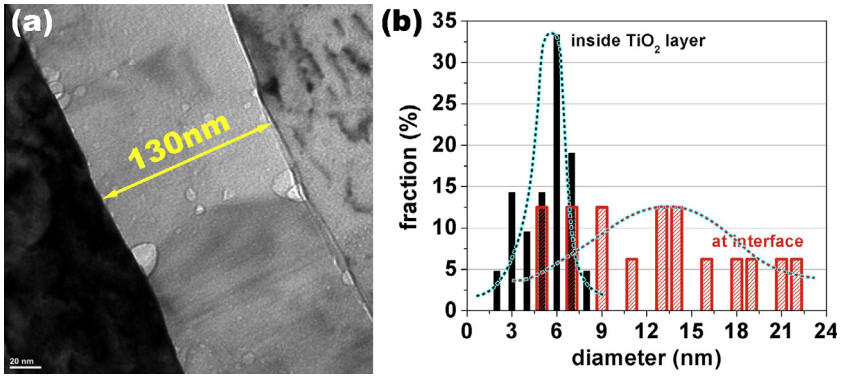

Fig. 6. (a) XTEM image showing the distribution of radiation generated voids in the oxide layer. (b) Corresponding size distribution of voids in the oxide layer, both within the interior of the oxide layer and at the interfaces.

are taken (either across amorphous or crystalline or void regions). The observed interdiffusion of Cr into the oxide is independent of interface OR. The EELS of the Ti $L_{2,3}$-edge was captured throughout the oxide layer (Fig. 7d) and the valence state of Ti does not change significantly after irradiation [39].

4. Discussion

Our experimental results reveal two surprising aspects of the behavior of Cr at $FeCr/TiO_{2-x}$ interfaces. First, upon irradiation, Cr penetrates the entire oxide layer. Second, upon incorporation of Cr, the rutile structure is much more

susceptible to amorphization than before. We discuss the origins of this behavior in the following sections.

4.1. Cr diffusion

In our study, both EDS and EELS mapping analysis were performed to investigate the evolution of the composition profiles across the interface. Comparison of the shape of the profiles at pristine, annealed and irradiated interfaces reveals that, during either high temperature annealing or irradiation, Cr diffuses across the metal/oxide interface. *Ab-initio* calculations suggest that Cr is the faster diffusing species within the Fe matrix at all temperatures both for vacancy and interstitial diffusion mechanisms, compared to the matrix bcc Fe [40]. Ion irradiations produce high concentration of point defects in solids; while most of the defects simply recombine, the remaining concentration of vacancy-interstitial pairs in the lattice is still large. The initial FeCr/TiO_{2-x} interface is acting as a strong sink to absorb those defects. Due to the lower migration barriers of Cr atoms and stronger coupling with vacancies, Cr reaches the interface much earlier than Fe. Meanwhile, the higher affinity for oxygen of Cr than Fe may provide another driving force to drag Cr toward oxide. Thus, there is a net flow of Cr toward the interface, a flow that is enhanced under irradiation because of the excess defect concentrations.

Surprisingly, however, no accumulation of Cr was observed at the metal/oxide interface. Instead, Cr diffuses into and spreads throughout the whole TiO_2 layer under irradiation. Since the oxygen affinity of Cr is much less than that of Ti, the observed phenomenon of rapid diffusing of Cr into TiO_2 is believed to be related to the oxygen deficient TiO_2 phase and high density of GBs. To understand the thermodynamics of Cr substitution into rutile TiO_{2-x}, we calculated the formation energy of substitutional Cr or Fe atoms at Ti sites in stoichiometric and substoichiometric rutile TiO_2. Since, both Fe and Cr have similar radii to Ti, a substitutional position is most favorable. The formation energy for substituting Cr (Fe) into stoichiometric titania Cr–TiO_2 (Fe–TiO_2) and sub-stoichiometric titania Cr–TiO_{2-x} (Fe–TiO_{2-x}) were calculated using the equations below:

$$F(Cr-TiO_2) = \mu_{Ti} + E(CrTi_{23}O_{48}) + E(Fe_{23}) - E(Fe_{23}Cr) - E(Ti_{24}O_{48}) \quad (1)$$

$$F(Fe-TiO_2) = \mu_{Ti} + E(FeTi_{23}O_{48}) + E(Fe_{23}) - E(Fe_{24}) - E(Ti_{24}O_{48}) \quad (2)$$

$$F(Cr-TiO_{2-v}) = \mu_{Ti} + E(CrTi_{23}O_{47}) + E(Fe_{23}) - E(Fe_{23}Cr) - E(Ti_{24}O_{47}) \quad (3)$$

$$F(Fe-TiO_{2-v}) = \mu_{Ti} + E(FeTi_{23}O_{47}) + E(Fe_{23}) - E(Fe_{24}) - E(Ti_{24}O_{47}), \quad (4)$$

where $E(CrTi_{23}O_{48})$ and $E(FeTi_{23}O_{48})$ are the DFT calculated energies of supercells with one Ti atom replaced by either Cr and Fe, respectively, in $Ti_{24}O_{48}$. $E(Fe_{23}Cr)$ is the DFT calculated energy of supercell with Cr sitting at lattice site of Fe in bcc Fe. In these equations, Cr in Fe is assumed to form a solid solution in Fe–Cr layer. $E(Ti_{23}O_{47})$ is the DFT calculated energy of a supercell of titania containing one oxygen vacancy. Fig. 8 shows the substitutional defect formation energy of Cr and Fe in both stoichiometric and sub-stoichiometric titania as a function of the Ti chemical potential, in rutile and anatase phases. The behavior in both phases of TiO_{2-x} is very similar.

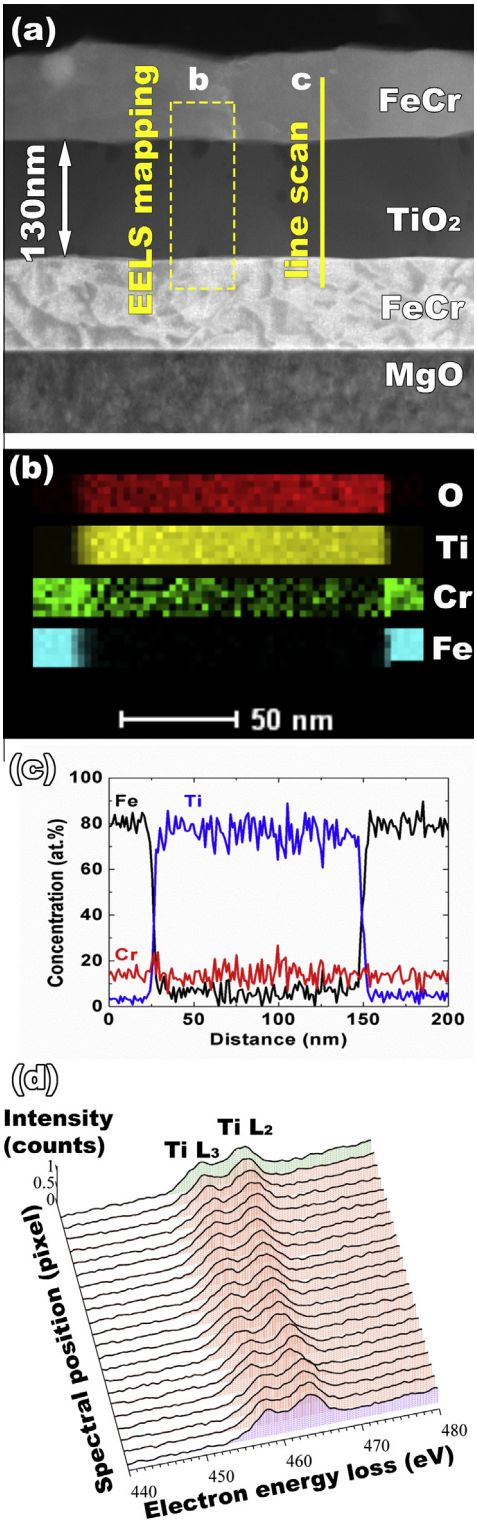

Fig. 7. (a) Dark field STEM image of irradiated multilayers. (b) EELS and (c) EDS chemical analyses indicate the diffusion of Cr throughout the virgin oxide layer following irradiation. (d) EELS of the Ti $L_{2,3}$-edge throughout the oxide layer.

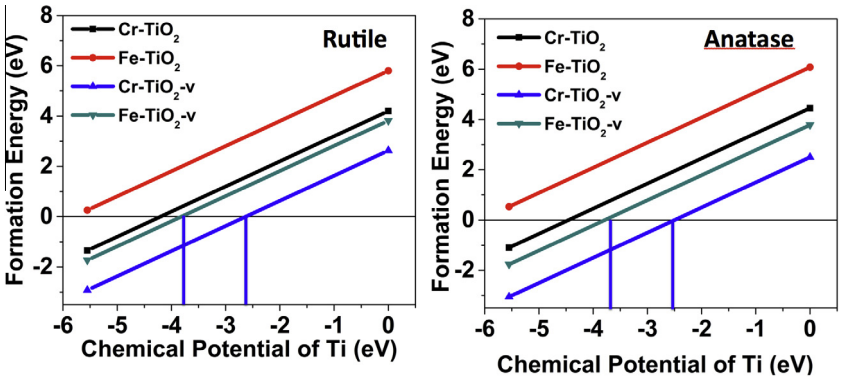

Fig. 8. Substitutional defect formation energy of Cr (Fe) in stoichiometric titania Cr–TiO_2 (Fe–TiO_2) and sub-stoichiometric titania Cr–TiO_{2-x} (Fe–TiO_{2-x}) as a function of the Ti chemical potential, in rutile and anatase phases.

For all chemical potentials of Ti, Cr substitution into TiO_{2-x} is easier, regardless of stoichiometry, than Fe. However, there is also a window of chemical potential in which that substitution is thermodynamically favorable, specifically in sub-stoichiometric TiO_{2-x}. That is, for TiO_{2-x}, there is a regime in which Cr substitution into TiO_{2-x} is exothermic while Fe substitution is endothermic, as indicated by the vertical lines. The highest chemical potential of Ti is for Ti in a bulk metallic state while the lowest corresponds to atomic Ti. The chemical potential of Ti that establishes equilibrium between TiO_2 and Ti_2O_3 (one of the sub-stoichiometric TiO_2 phase) is −1.98 eV. This value falls between the two extreme chemical potentials considered. For any given chemical potential of Ti, of the four reactions, it is always easiest to create Cr substitutional defects in substoichiometric titania. This is because the trivalent Cr ion, which would normally be accommodated by the formation of oxygen vacancies in stoichiometric titania to ensure charge neutrality, already has those vacancies present in substoichiometric titania. These results provide a qualitative explanation for both why Cr interpenetration into TiO_2 is much easier in sub-stoichiometric TiO_{2-x} than stoichiometric TiO_2 and why Fe incorporation is not as prevalent as Cr substitution.

Regarding the actual diffusion mechanism of Cr into the oxide layer, three possible phenomena may occur: (i) Cr may dissolve substitutionally and diffuse via an interstitial mechanism [41,42]. Generally, in rutile, interstitial species (Ti_i and O_i) have significantly lower migration barriers as compared to vacancy species (V_{Ti} and V_O), leading to faster diffusion [41]. Due to the electronic structure of the trivalent Cr ion, it is probable for Cr to dissolve substitutionally and diffuse by the simultaneous and cooperative motion of Ti and Cr ions [42]. (ii) The high density of GBs in the oxide layer may provide a fast diffusion channel for Cr, at least initially [43]. (iii) Considering the observation of a large number of voids formed in oxide after irradiation, another alternative mechanism that may be at work here is Cr may diffuse through a vacancy exchange mechanism into oxide. Similar phenomenon was reported in irradiated nanosized rutile [44]. At this time, we cannot eliminate any of these possibilities. However, the fact that the Cr distribution in the titania layers appears to be homogenous both after annealing and after irradiation suggests that the GB mechanism is not likely dominant as one would then expect higher concentrations of Cr at GBs. Further, because Cr incorporation into titania is seen for both annealing and irradiation conditions suggests that interstitials, which are unlikely in the thermal system, are not the dominant mechanism. Together, this implies that mechanism iii, the vacancy exchange mechanism, likely is the dominant one.

One other point is worth noting. In both the annealed and irradiated samples, Cr diffuses into the titania layer, but the Cr penetration depth is much greater for the irradiated sample. At the same time, there is no accumulation of Cr at the metal/oxide interface. This suggests that the rate limiting step for Cr incorporation into titania is the diffusion of Cr in the Fe matrix to the interface. The primary difference between the irradiated and annealed sample is the arrival rate of Cr to the interface, which is enhanced under irradiation due to the higher concentration of defects, particularly interstitials. Finally, we note that Cr incorporation into titania will further drive the oxide to sub-stoichiometry. Mass conservation implies that the material will get less dense and thus expand, consistent with the experimental observations of swelling of the oxide layer. Of course, the swelling may also be due to the amorphization transformation of the oxide.

4.2. Cr enhanced amorphization

Irradiation-induced amorphization is often attributed to the accumulation of radiation damage in a lattice, which then collapses into an amorphous structure when it reaches a critical defect density [45]. Typically, there exists a critical temperature above which it is no longer possible to amorphize the given compound, due to the fact that the thermal reordering rate will exceed the damage rate as the temperature rises. Compared to other polymorphs of titania, rutile is known to be the most amorphization-resistant [46–48]. Hartmann showed that under heavy ion irradiation, single crystal rutile only amorphizes at temperatures below 200 K [49]. However, in our study, the amorphization of TiO_{2-x} was realized under irradiation at the relatively high temperature of 773 K. Based on the observation of Cr diffusion into the TiO_{2-x} layer, our hypothesis is that incorporation of Cr is the major reason for accelerating this amorphization process. Due to the similar ionic radii between Cr and Ti (0.61 Å for Ti^{4+} and 0.62 Å for Cr^{3+} in octahedral coordination) and the pre-existing oxygen vacancies in substoichiometric titania, Cr is able to occupy regular cation positions leading to a substitutional solid solution that maintains the

electroneutrality of the structure [50]. With Cr atoms incorporating into TiO_{2-x}, the bonding strength between metal and oxygen ions will be suppressed, which may induce greater production of point defects under irradiation by effectively lowering the displacement threshold energy in the doped material. On the other hand, Lumpkin et al. [51] also reported that the presence of impurities dramatically increased the amorphous transition temperature of rutile, which they attributed to the capturing of charged irradiation-induced defects by the aliovalent dopant cation. Thus, adding Cr to TiO_2 may increase the production of point defects as well as retard the recombination processes, both of which lead to higher concentrations of defects and more susceptibility for amorphization. However, at this time, both of these hypotheses are conjectures and warrant further study to precisely understand the role of Cr on the amorphization resistance of TiO_2.

5. Summary

In summary, FeCr/TiO_{2-x}/FeCr trilayer thin films were subjected to either annealing at 500 °C for 1 h or 10 MeV Ni^{3+} ion irradiation at 500 °C. Diffusion of Cr from the Fe layers into the TiO_{2-x} layer, with negligible accumulation at the FeCr/TiO_{2-x} interface, was observed in both cases. Cr preferentially diffuses into the oxygen-deficient titania as compared to segregation at metal/oxide interfaces. The rate at which the Cr concentration increases in titania appears to be limited by the diffusion of Cr to the interface from the Fe matrix. The extent of Cr interdiffusion is much larger in the case of the ion irradiated sample, pointing to the role of radiation-induced defects in enhancing the transport of Cr both to the interface and into the oxide. First-principles calculations show that it is thermodynamically favorable to substitute Ti with Cr in sub-stoichiometric TiO_2, consistent with the experimental results. Additionally, diffusion of Cr into the oxide layer changes the bond nature of tetragonal rutile crystal structure and enhances amorphization under irradiation. The observed phenomena of Cr incorporation into and Cr enhanced amorphization of rutile are independent of the interface orientation relationship, at least for the current irradiation conditions.

Acknowledgements

We gratefully acknowledge the support of the U.S. Department of Energy through the Los Alamos National Laboratory (LANL)/Laboratory Directed Research & Development (LDRD) Program for this work. This research used resources provided by the LANL Institutional Computing Program. This work was performed, in part, at the Center for Integrated Nanotechnologies, an Office of Science User Facility operated for the U.S. Department of Energy (DOE) Office of Science. LANL, an affirmative action/equal opportunity employer, is operated by Los Alamos National Security, LLC, for the National Nuclear Security Administration of the U.S. Department of Energy under contract DE-AC52-06NA25396. JAA acknowledges access to the ORNL's ShaRE User Facility where part of the TEM work was performed in collaboration with Miaofang Chi and Juan Carlos Idrobo, which is sponsored by the Scientific User Facilities Division, Office of Basic Energy Sciences, U.S. Department of Energy. Y. Xu and H. Luo are CMIME affiliates supported by the New Mexico Consortium and LANL.

References

[1] A.J. Ardell. Materials Issues for Generation IV Systems 2008, 285.
[2] H. Wiedersich, P.R. Okamoto, N.Q. Lam, J. Nucl. Mater. 83 (1979) 98.
[3] T.R. Allen, G. Was, Acta. Mater. 46 (1998) 3679.
[4] M. Nastar, F. Soisson, in: Rudy J.M. Konings, (Ed.), Comprehensive Nuclear Materials, Elsevier, vol. 1, 2011, pp. 471.
[5] I.-W. Chen, J. Nucl. Mater. 116 (1983) 249.
[6] K.G. Field, L.M. Barnard, C.M. Parish, J.T. Busby, D. Morgan, T.R. Allen, J. Nucl. Mater. 435 (2013) 172.
[7] G. Was, B.D. Wirth. Award Number: DE-FC07-07ID14828, 2011.
[8] J.P. Wharry, Z. Jiao, G.S. Was, J. Nucl. Mater. 425 (2012) 117.
[9] G.S. Was, J.P. Wharry, B. Frisbie, B.D. Wirth, D. Morgan, J.D. Tucker, T.R. Allen, J. Nucl. Mater. 411 (2011) 41.
[10] Z. Lu, R.G. Faulkner, G. Was, B.D. Wirth, Scr. Mater. 58 (2008) 878.
[11] P.J. Maziasz, J. Nucl. Mater. 169 (1989) 95.
[12] J.T. Busby, G. Was, E.A. Kenik, J. Nucl. Mater. 302 (2002) 20.
[13] J. Mulroue, B.P. Uberuaga, D.M. Duffy, J. Phys.: Condens. Matter 25 (2013) 065502.
[14] O. Anderoglu, M.J. Zhou, J. Zhang, Y.Q. Wang, S.A. Maloy, J.K. Baldwin, A. Misra, J. Nucl. Mater. 435 (2013) 96.
[15] Y. Chen, L. Jiao, C. Sun, M. Song, K.Y. Yu, Y. Liu, M. Kirk, M. Li, H. Wang, X. Zhang, J. Nucl. Mater. 452 (2014) 321.
[16] M. Polak, J. Vac. Sci. Technol. A 5 (1987) 590.
[17] S. Choudhury, J.A. Aguiar, M.J. Fluss, L.L. Hsiung, A. Misra, B.P. Uberuaga, Sci. Rep. (submitted for publication).
[18] J. Ribis, M.L. Lescoat, Y. de Carlan, J.M. Costantini, I. Monnet, T. Cozzika, F. Delabrouille, J. Malaplate, J. Nucl. Mater. 417 (2011) 262.
[19] S. Yamashita, N. Akasaka, S. Ukai, S. Ohnuki, J. Nucl. Mater. 367–370 (2007) 202.
[20] T.R. Allen, J. Gan, J.I. Cole, M.K. Miller, J.T. Busby, S. Shutthanandan, S. Thevuthasan, J. Nucl. Mater. 375 (2008) 26.
[21] G.R. Odette, M.J. Alinger, B.D. Wirth, Annu. Rev. Mater. Res. 38 (2008) 471.
[22] A. Hirata, T. Fujita, Y.R. Wen, J.H. Schneibel, C.T. Liu, M.W. Chen, Nat. Mater. 10 (2011) 922.
[23] C.A. Williams, P. Unifantowicz, N. Baluc, G.D.W. Smith, E.A. Marquis, Acta Mater. 61 (2013) 2219.
[24] J. Ciston, Y. Wu, G. Odette, P. Hosemann, Microsc. Microanal. 18 (2012) 760.
[25] E.A. Marquis, Appl. Phys. Lett. 93 (2008) 181904.
[26] E.A. Marquis, S. Lozano-Perez, V.D. Castro, J. Nucl. Mater. 417 (2011) 257.
[27] D. Bhattacharyya, P. Dickerson, G.R. Odette, S.A. Maloy, A. Misra, M.A. Nastasi, Philos. Mag. 92 (2012) 2089.
[28] N. Sakaguchi, S. Watanabe, H. Takahashi, Nucl. Instrum. Methods B 153 (1999) 142.
[29] M.J. Zhuo, E.G. Fu, L. Yan, Y.Q. Wang, Y.Y. Zhang, R.M. Dickerson, B.P. Uberuaga, A. Misra, M. Nastasi, Q.X. Jia, Scripta Mater. 65 (2011) 807.
[30] M.J. Demkowicz, R.G. Hoagland, B.P. Uberuaga, A. Misra, Phys. Rev. B 84 (2011).
[31] J.F. Ziegler, J.P. Biersack, Calculation using the Stopping and Range of Ions in Matter (SRIM) code, 2008 <www.srim.org>.
[32] G. Kresse, J. Hafner, Phys. Rev. B 47 (1993) 558.
[33] G. Kresse, J. Hafner, Phys. Rev. B 49 (1994) 14251.
[34] J.P. Perdew, K. Burke, M. Ernzerhof, Phys. Rev. Lett. 77 (1996) 3865.
[35] J.K. Burdett, T. Hughbanks, G.J. Miller, J.W. Richardson, J.V. Smith, J. Am. Chem. Soc. 109 (1987) 3639.

[36] A. Benyoucef, A. Benyoucef, F. Lapostolle, D. Klein, B. Benyoucef, Revue des Energies Renouvelables ICRESD-07 Tlemcen, 2007, 61.
[37] C.H. Heo, S.-B. Lee, J.-H. Boo, Thin Solid Films 475 (2005) 183.
[38] M.D. Wiggins, M.C. Nelson, C.R. Aita, J. Vac. Sci. Technol. A 14 (1996) 772.
[39] J.A. Aguiar, P.P. Dholabhai, Z. Bi, Q. Jia, E.G. Fu, Y.Q. Wang, T. Aoki, J. Zhu, A. Misra, B.P. Uberuaga, Adv. Mater. Interfaces 1 (2014) 1300142.
[40] S. Choudhury, L. Barnard, J.D. Tucker, T.R. Allen, B.D. Wirth, M. Asta, D. Morgan, J. Nucl. Mater. 411 (2011) 1.
[41] B.P. Uberuaga, X.M. Bai, J. Phys.: Condens. Matter 23 (2011) 435004.
[42] J. Sasaki, N.L. Peterson, K. Hoshino, J. Phys. Chem. Solids. 46 (1985) 1267.
[43] X.-M. Bai, B.P. Uberuaga, Philos. Mag. 92 (2012) 1469.
[44] J. Zhang, J. Lian, F. Namavar, J. Wang, H. Haider, K. Garvin, R.C. Ewing, J. Phys. Chem. C 115 (2011) 22755.
[45] K.C. Russell, Prog. Mater. Sci. 28 (1984) 229.
[46] B.P. Uberuaga, X.-M. Bai, J. Phys.: Condens. Matter 23 (2011) 435004.
[47] D. Yarotski, E. Fu, L. Yan, Q. Jia, Y. Wang, A.J. Taylor, B.P. Uberuaga, Appl. Phys. Lett. 100 (2012) 251603.
[48] G.R. Lumpkin, M.G. Blackford, K.L. Smith, K.R. Whittle, N.J. Zaluzec, E.A. Ryan, P. Baldo, Am. Mineral 95 (2009) 192.
[49] T. Hartmann, L.M. Wang, W.J. Weber, N. Yu, K.E. Sickafus, J.N. Mitchell, C.J. Wetteland, M.A. Nastasi, M.G. Hollander, N.P. Baker, C.R. Evans, J.R. Tesmer, C.J. Maggiore, Nucl. Instrum. Methods B 141 (1998) 398.
[50] A. Escudero, F. Langenhorst, J. Solid State Chem. 190 (2012) 61.
[51] G.R. Lumpkin, M.G. Blackford, K.L. Smith, K.R. Whittle, N.J. Zaluzec, E.A. Ryan, P. Baldo, Am. Mineral 95 (2010) 192.